

# Analysis of flexural capacity of a novel straight-side U-shaped steel-encased concrete composite beam

Qiwu Yan<sup>a</sup>, Zheng Zhang<sup>a</sup>, Jin Yan<sup>b,\*</sup>, Simon Laflamme<sup>b</sup>

<sup>a</sup>*School of Civil Engineering, Central South University, Changsha, China;*

<sup>b</sup>*Department of Civil, Construction, and Environmental Engineering, Iowa State University, Ames, IA, USA*

---

## Abstract

This paper proposes a novel straight-side U-shaped steel-encased concrete composite beam (SUSCCB). The SUSCCB is constituted by encasing the top sections of the U-shaped steel plates directly into the concrete flange, with the composite action generated through perfbond connections consisting of reinforcement bars transversely passing through perforations in the encased top sections of the steel plates. It is engineered to overcome the shortcomings of the existing varus or valgus U-shaped steel-encased concrete composite beams (USCCB), for which the installation of shear connectors can be complex and costly to achieve because of the numerous required welds. The main objective of this paper is to study the flexural behavior of the proposed SUSCCB and develop a method for calculating its flexural capacity. A finite element model (FEM) is developed and validated against available USCCB experimental results. After, the validated FEM is used to conduct a parametric study of the SUSCCB. The flexural behavior is assessed from the strain distribution, stress analysis, and load-deflection curves. Results show that the flexural performance of the SUSCCB is superior to that of a traditional USCCB, and that its flexural capacity can be calculated through the simplified plastic theory. Lastly, the analytical flexural capacity of the SUSCCB is derived. The analytical values show close agreement with results from the numerical simulations.

**Keywords:** U-shaped steel, flexural capacity, section plasticity theory, finite element analysis

---

## 1. Introduction

U-shaped steel-encased concrete composite beams (USCCB) have been widely used and often deployed in the form of long span beams for tall structures and bridges to improve structural capacity and cost efficiency. For example, they have been used for the extra-long transition beams in the Guangzhou pearl river new town F2-4 block tall building [1], the Tower Building of Beijing Yintai Center [2], and the main beam of Nanchang Yingxiong Bridge [3]. A USCCB consists of a U-shaped cold-formed thin-walled steel component infilled with concrete to form the web, and with a concrete flange poured onto the web to create a final T-section, using the necessary shear connectors to generate the composite action. For long-span USCCB, the U-shaped steel beam needs to be completely filled with concrete to reduce or eliminate local buckling, and to create a composite effect to improve flexural and shear capacity. Remark that for smaller spans, it is possible to use non-filled U-shaped steel beams, but this is out-of-the-scope of the paper.

Existing USCCBs can be divided into two sub-types based on the shape of the top flange: varus-type (Fig. 1(a)) [4, 5] and valgus-type (Fig. 1(b)) [6, 7, 8] top flanges. USCCB sections possess many advantages, such as: (1) reducing or eliminating local buckling of the thin-walled external steel plate through the restraint created by the encased concrete [9, 10]; (2) providing superior fire resistance and preventing transient heat transfer when the encased concrete is wet [11], with the longitudinal reinforcement bars in the web acting

---

\*Corresponding author

Email addresses: yaqwu@csu.edu.cn (Qiwu Yan), zhangzheng9617@csu.edu.cn (Zheng Zhang), yanjin@iastate.edu (Jin Yan), laflamme@iastate.edu (Simon Laflamme)

as the second line of defense if the steel plates were to fail at high temperatures; and (3) providing a higher shear capacity through the composite action [12, 13, 14].

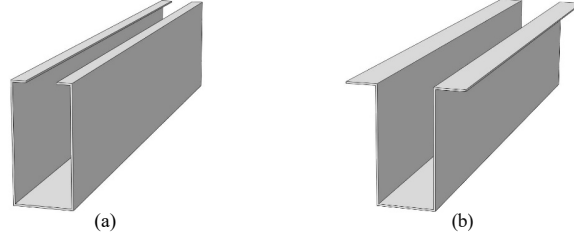


Figure 1: Typical types of existing steel U-sections: (a) varus-type; and (b) valgus-type top flanges.

The overall behavior of a USCCB strongly depends on the shear connection between the steel plate and the concrete flange. For the valgus-type top flange USCCB, the most popular shear connectors are headed studs and short channels [15, 16, 17, 18]. Recently, Liu [19] and Keo [20] studied a USCCB equipped with equal-leg angles welded along the transverse direction to the steel plates. Liu's experimental results showed that composite beams with angle connectors welded to the webs of U-shaped steel plate failed in a brittle mode, while composite beams with angle connectors welded on the top flange of U-shaped steel failed in a ductile mode. Keo developed a finite element model (FEM) to identify the stress behavior of the equal-leg angle connectors and the surrounding concrete. Based on the results of the parametric study, an analytical formula for calculating the force transfer capacity of the shear connector was developed. For the varus-type top flange USCCB, Zhou's research group investigated the flexural behavior [21, 22], shear behavior [23], and torsional behavior [24] of a novel cold-formed U-shaped steel-concrete composite beam constituted using a truss-type and inverted U-shaped reinforcement bar system.

Although existing USCCBs have shown excellent mechanical properties and promising engineering applications, they have noticeable shortcomings. Firstly, headed studs, channels, and/or angle connectors all require a significant number of welds, with a risk of through-penetration for thin components. Secondly, the installation of these connectors requires special tools and skilled operators, resulting in additional costs. Thirdly, it is difficult to bend valgus-type or varus-type top flanges at 90-degree. Lastly, the varus-type top flange requires a number of open holes to create access points for concrete vibrators when casting the web.

In consideration of the shortcomings of the existing varus-type or valgus-type USCCBs, this paper proposed a novel straight-side U-shaped steel-encased concrete composite beam (SUSCCB). The SUSCCB is constituted by encasing the top sections of the U-shaped steel plates directly into the concrete flange ("connector" in Fig. 2(d)), with the composite action generated through perfobond connections consisting of reinforcement bars transversely passing through perforations in the encased top sections of the steel plates. The SUSCCB is illustrated in Fig. 2(a). Fig. 2(b) shows a typical cross-section of the novel SUSCCB, and Fig. 2(c) shows the front elevation view of the U-shaped steel. The perforations used in creating perfobonds between the flange and web are shown in Fig. 2(d). When the height permits, headed studs may be welded onto the bottom plate of the U-shaped steel to strengthen the composite action between the U-shaped steel and the concrete web. A SUSCCB has the following features: (1) the upper straight sides of the U-section improve the connection between the web and flange and provides stability during the beam's construction phase; (2) the perfobond connectors have adequate capacities against uplifting and slipping [25, 26, 27] between the concrete flange and the lower section that includes the U-shaped steel plate, encased concrete, and web reinforcement bars; (3) the straight-sided U-section is simple to fabricate compared to varus- and valgus-type U-sections; and (4) it only requires a relatively small number of welds between the headed studs and the bottom steel plate. Given these features, a SUSCCB is significantly faster and less expensive to fabricate compared with traditional USCCBs.

The main objective of this paper is to study the flexural behavior of the proposed SUSCCB and develop a method for calculating its flexural capacity. A three-dimensional FEM is developed and validated against experimental test data obtained on a varus-type U-shaped steel-encased concrete composite beam

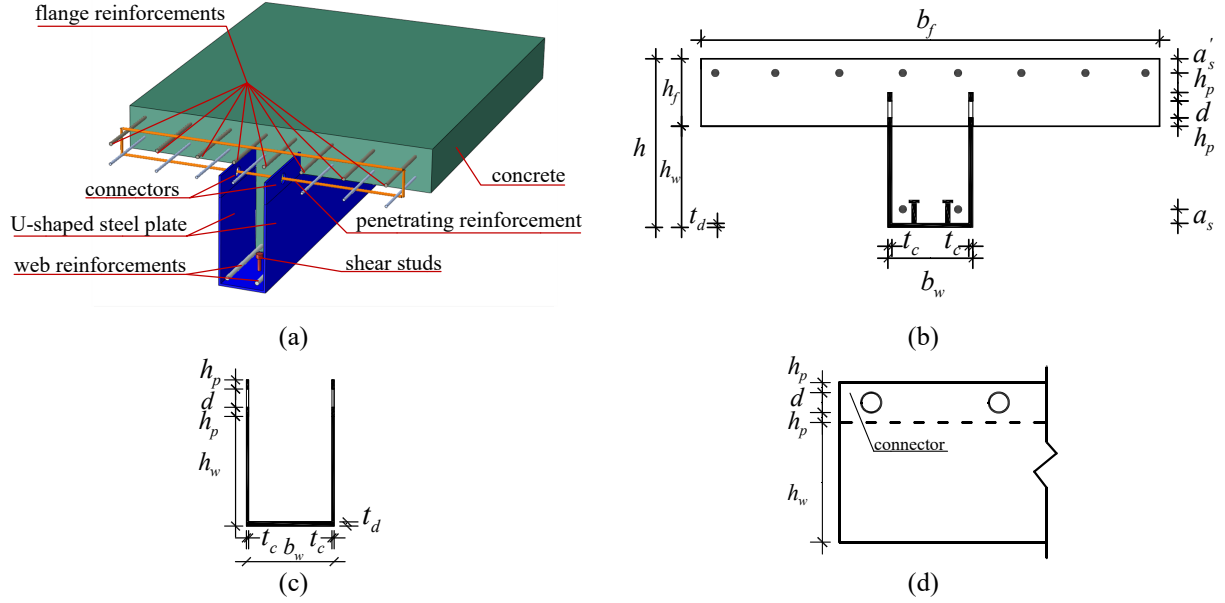


Figure 2: Details of a SUSCCB: (a) three-dimensional model; (b) typical cross-section; (c) U-shaped steel (front view); and (d) U-shaped steel (side view). ( $h$  is the beam height,  $h_f$  and  $b_f$  are the flange height and width, respectively;  $h_w$  and  $b_w$  are the web height and width, respectively;  $t_c$  and  $t_d$  are the side panel and bottom panel thicknesses, respectively;  $d$  is the opening diameter of connector batten;  $h_p$  is the height of the top or lower connector batten; and  $a_s$  and  $a'_s$  are the minimum distances between resultant forces of the reinforcement bar in the web and flange to the edge of the concrete, respectively.)

(VUSCCB) [28]. The validated model is used to conduct a parametric study of the proposed SUSCCB. The influence of the diameter and strength of the longitudinal reinforcement bars located in the web and flange, thickness and strength of the steel plates (i.e., thickness of the lateral and bottom plates, strength of steel), standard value of concrete strength, flange sectional dimensions (i.e., flange depth and width), and web sectional dimensions (i.e., web depth and width) is investigated. Results from the numerical investigation are used to suggest a methodology to compute the flexural capacity based on simplified plastic theory [29].

## 2. Finite element model

An FEM of the SUSCCB was created in ABAQUS 6.9 [30], and its specialization for modeling VUSCCB specimens was validated against experimental test results. A two-span symmetrical mid-monotonic loading is used to study the strength, stiffness and stability of the structure. The analytical method based on mechanics is used to measure the structure's response under static load, analyze, and evaluate the structure's stresses, behavior, and reliability. In this section, the VUSCCB experimental specimens are introduced, followed by the numerical modeling methods and a comparison of results.

### 2.1. Experimental specimens

Fig. 3(a) is a schematic of the configuration and reinforcement distribution details of a VUSCCB cross-section. Three specimens were tested each with different longitudinal reinforcement bar diameters: 6 mm (specimen B1), 10 mm (specimen B2), and 14 mm (specimen B3) running along the top flange, while the longitudinal reinforcement bar diameter at the bottom was kept constant at 6 mm. Each specimen includes two web reinforcement bars of 6 mm in diameter. The configuration and dimensions of the various U-shaped steel are shown in Figs. 3(b) and (c). The bottom headed studs are 50 mm high with a diameter of 16 mm and 160 mm spacing along the longitudinal direction. Each specimen has two 3000 mm spans with a total length of 6000 mm, as shown in Fig. 3(d).

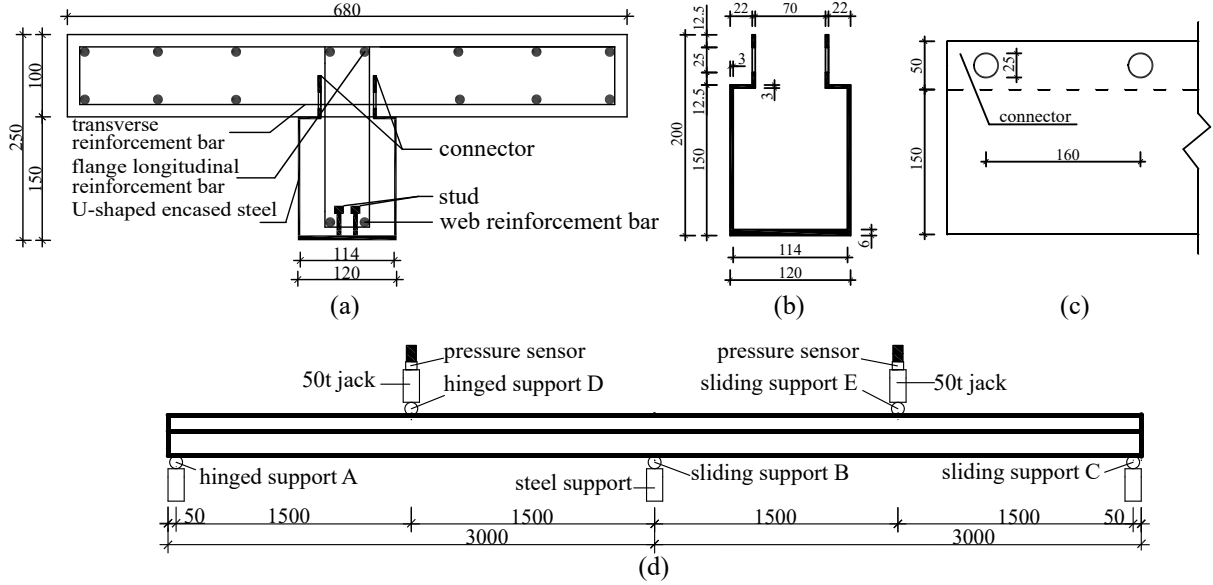


Figure 3: Details of the tested VUSCCB specimen (dimensions in mm): (a) typical cross-section; (b) U-shaped steel (front view); (c) U-shaped steel (side view); and (d) elevation view of the test model.

Table 1: Measured material properties.

Material	Diameter/thickness (mm)	Yield strength (MPa)	Ultimate strength (MPa)	Elongation (%)
Reinforcement bar	6	390	625	36
	10	380	600	28
	14	365	580	25
Steel	3	466	654	16
	6	465	660	18

Table 1 lists the properties of reinforcement bars and steel components obtained from tests [31]. The nominal yield and ultimate tensile strengths of the steel used for headed shear studs are 322 MPa and 410 MPa, respectively. The compressive strength of concrete is taken as 50.8 MPa, obtained from tests. Note that the properties of the studs were not experimentally verified.

## 2.2. Numerical model

### 2.2.1. Material constitutive model

The concrete constitutive model provided in literatures [20, 32] is used in the ABAQUS model. The uniaxial compressive stress-strain curve has the three segments shown in Fig. 4(a): (1) the first segment is assumed to be elastic when the stress is smaller than  $0.4f_c$ , where  $f_c$  is the compressive cylinder strength of concrete; (2) the second segment is a nonlinear parabolic curve starting at the proportional limit stress  $0.4f_c$  and ending at the peak stress  $f_c$ ; and (3) the third segment is a nonlinear decreasing curve starting at the peak stress  $f_c$ . Fig. 4(b) shows the tensile stress-crack width curve, where  $f_t = 0.3(f_c - 8)^{2/3}$  is the tensile strength.

The stress-strain relationship of the U-shaped steel and reinforcement bars is modeled using the elastic-plasticity constitutive model recommended by Ding [33], and the strength criterion modeled using the Mises yield criterion and associated flow rule.

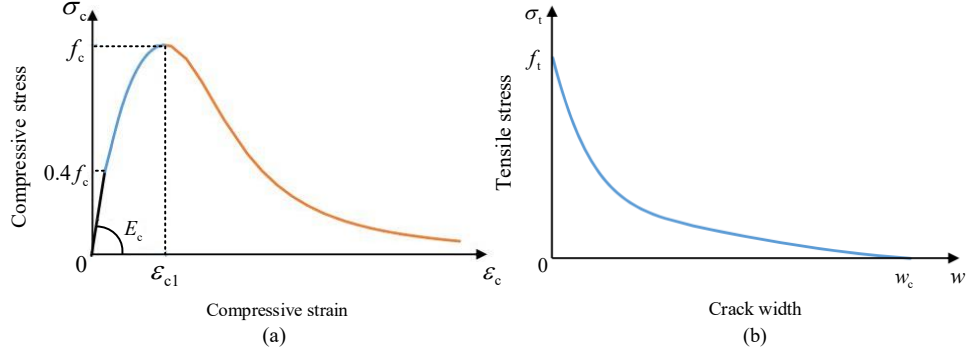


Figure 4: Concrete constitutive model: (a) compression; and (b) tension.

### 2.2.2. Contact interactions

There are tangential and normal effects on the contact surface between the U-shaped steel plate and encased concrete. All contact surfaces are assumed, by default, to have a normal behavior (i.e., hard contact). After, the penalty friction formulation is used to characterize the tangential behavior between the U-shaped steel plate and encased concrete with a coefficient of friction equal to 0.3 [20]. An embedded constraint is applied for the reinforcement bars and studs placed inside the encased concrete. The surfaces in contact between the loading plates (hypothetical materials with high stiffness where the load is applied) and concrete are assumed to be perfectly bonded without slippage [34, 35].

### 2.2.3. Element types and meshing

The concrete material is discretized with a uniform mesh of solid elements C3D8R. The U-shaped steel is discretized with 4-node shell elements S4R (using the Simpson's integral of 9 nodes along the thickness of the shell element). The reinforcement bars are modeled using the two-node linear and three-dimensional truss element T3D2, while the studs are modeled using the linear beam element B31. All components are modeled with a similar mesh size, as depicted in Fig. 5.

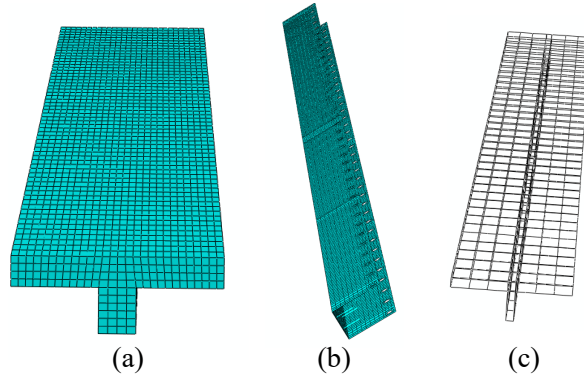


Figure 5: VUSCCB FEM for a typical specimen: (a) concrete; (b) steel and studs; and (c) reinforcing cage.

### 2.2.4. Loading and boundary conditions

Fig. 6 shows the loading and boundary conditions of a typical VUSCCB FEM. The bottom edge at the left support is fixed against all displacements (x, y, and z directions), and the middle and right support bottom edges are both fixed against lateral displacements (x and y directions) and only allowing longitudinal rotation along the x-axis. Displacement-controlled loading is applied at the two mid spans symmetrically in y-axis.

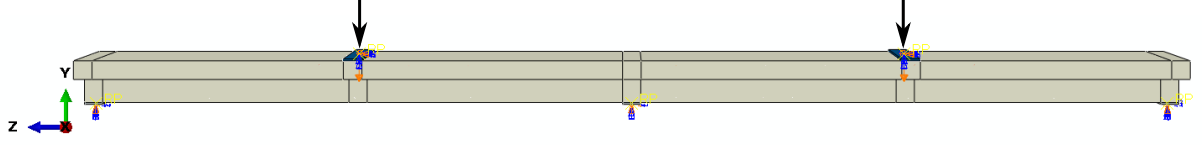


Figure 6: Loading and boundary conditions of the FEM.

### 2.3. Comparison and verification

The load-deflection curves from the numerical models were compared with those from the three VUSCCB experimental specimens, plotted in Fig. 7. The numerical model outputted yield load  $P_{ny}$ , yield displacement  $\Delta_{ny}$  (data from universal yield moment method [36]), peak load  $P_{nmax}$ , and peak displacement  $\Delta_{nx}$ , show very close agreement with the corresponding experimental results,  $P_y$ ,  $\Delta_y$ ,  $P_{max}$ , and  $\Delta_x$ . The experimental and numerical characteristic points of the load-deflection curves are listed and compared in Table 2. For all of the examined specimens, simulation results overestimate those from experimental results, with a maximum difference within 9.9% except at the peak displacement for the B1 composite beam where simulation results were underestimate by 7.4%. The differences between FEA curves and test results, being less than 10%, is acceptable [20].

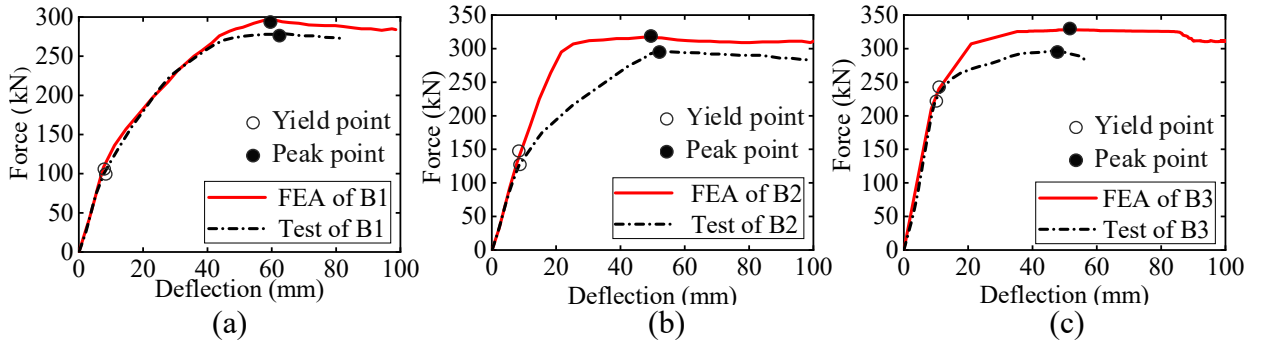


Figure 7: Comparison of numerical and experimental results for the three VUSCCB specimens: (a) B1; (b) B2; and (c) B3.

Table 2: Comparison of the numerical and experimental load-deflection characteristic points.

Specimen	Yield load (kN)		Diff (%)	Peak load (kN)		Diff (%)	Yield displacement (mm)		Diff (%)	Peak displacement (mm)		Diff (%)
	$P_y$	$P_{ny}$		$P_{max}$	$P_{nmax}$		$\Delta_y$	$\Delta_{ny}$		$\Delta_x$	$\Delta_{nx}$	
B1	94.5	100.7	6.5	278.2	298.2	7.2	7.8	8.3	5.4	63.7	59	-7.4
B2	127.1	130.2	2.4	296.6	315.1	6.3	8.1	8.3	3.3	50.5	52.9	4.7
B3	208	215.9	3.8	298.2	328	9.9	8.6	9.4	9.3	47.4	50.2	5.9

$$\delta_1 = (P_{ny} - P_y)/P_y, \delta_2 = (P_{nmax} - P_{max})/P_{nmax}, \delta_3 = (\Delta_{ny} - \Delta_y)/\Delta_y, \delta_4 = (\Delta_{nx} - \Delta_x)/\Delta_y.$$

Results from the three VUSCCB experimental specimens exhibited strong shear in the oblique section and weak bending in the normal section, resulting in a first batch of transverse cracks that formed on the upper surface of flange near mid-support, a rotation of the cross section of the mid-support while mid-span deflection increased, transverse cracks at the bottom of the mid-span and top of the mid-support developing rapidly and forming multiple transverse cracks, normal section bending failure of the mid-support section and mid-span section successively, and a main crack with a width of approximately 0.3 mm formed on

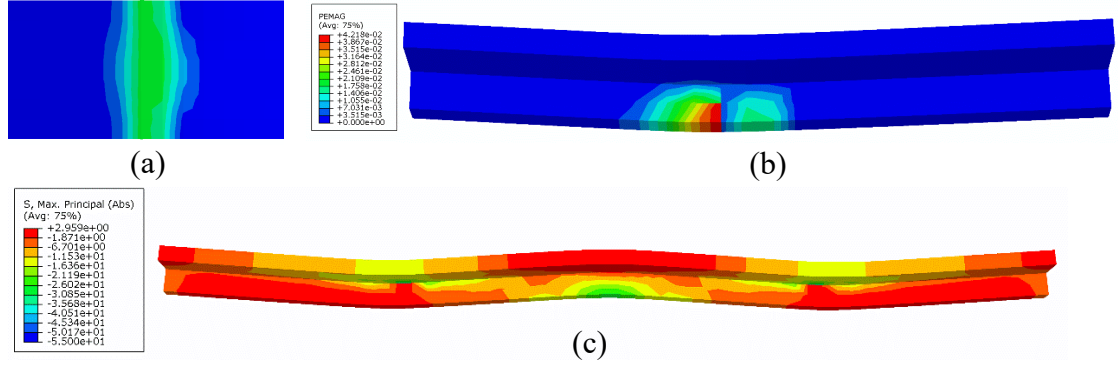


Figure 8: FEM outputs: (a) strain distribution at the upper surface of the concrete flange near mid-support; (b) strain distribution at the concrete web crack (smeared) near mid-span; and (c) stress distribution and deformation.

Table 3: Stress and strain values at section key loading points from FEM B1.

Point	$\sigma_{mbs}$	$\sigma_{sbs}$	$\sigma_{mts}$	$\sigma_{sts}$	$\sigma_{mtr}$	$\sigma_{mcr}$	$\sigma_{str}$	$\sigma_{scr}$	$\varepsilon_{mce}$	$\varepsilon_{sce}$
Yield	185.3	52.3	101.7	113.5	129.7	113.4	148.8	101.1	0.0007	0.0002
Peak	465	142.1	465	465	390.1	390.7	390.1	390.2	0.0033	0.0032

the top of the mid-support at failure. Figure 8 shows the load-deflection simulation results from the finite element analysis of the composite beam. Figures 8a and 8b show that transverse cracks are first formed on the upper surface of flange near the mid-support, then progress on the concrete web near mid-span. Figure 8c indicates mid-span deflection and mid-support rotation. The cracking and progression of cracks simulated by FEM of the composite beam is consistent with the experimental results. Stress and strain values at key loading points from FEM B1 are listed in Table 3. The stress of steel bar (6 mm) at yield is 390 MPa, the stress of steel plate at yield is 465 MPa; the peak pressure strain of concrete is approximately 0.002, and the ultimate pressure strain of concrete is approximately 0.0033. As it be seen from Table 3, when loading at peak load, the top and bottom of the steel plate at the mid-span section, the top of the steel plate at the mid-support section, and all of the tensile and compressive steel bars are yielding, the plastic development in the compressive concrete section is obvious, the edge strain of the compressive concrete is larger than the peak strain of the compressive concrete (0.002), and the ultimate compressive strain of the compressive concrete is close to or exceeds 0.0033. The failure from simulated FEM B1 is the bending failure of the normal section, which is consistent with the failure characteristics of composite beam test. The above comparisons in Fig. 7 and Table 2, and failure patterns and strain or stress developments in Figure 8 and Table 3, indicate that the FEM is valid to predict the flexural capacity and the initial stiffness of a VUSCCB. It follows that the same modeling procedure can be used to model and numerically investigate the proposed SUSCCB.

### 3. Parametric study on the SUSCCB

In this section, the validated FEM is specialized to study the behavior of the proposed SUSCCB through a parametric study. In particular, the flexural capacity in terms of beam dimensions and material properties is assessed. Parameters of interest are the diameters of the longitudinal reinforcement bars, the thickness of the U-shaped steel, the widths and depths of the web and flange, and the reinforcement bar and concrete strengths. The parametric study is divided into 11 groups as tabulated in Table 4. Each group has the same common dimensions as illustrated in Fig. 9 (ZHL1-1), except the varying parameters indicated. Results are benchmarked against the ZHL1-1 case. In total, 29 parametric variations are investigated. Load-deflection curves, strain, and stress data are obtained from the finite element simulations and analyzed. The

performance of the SUSCCB is also compared against that of the VUSCCB.

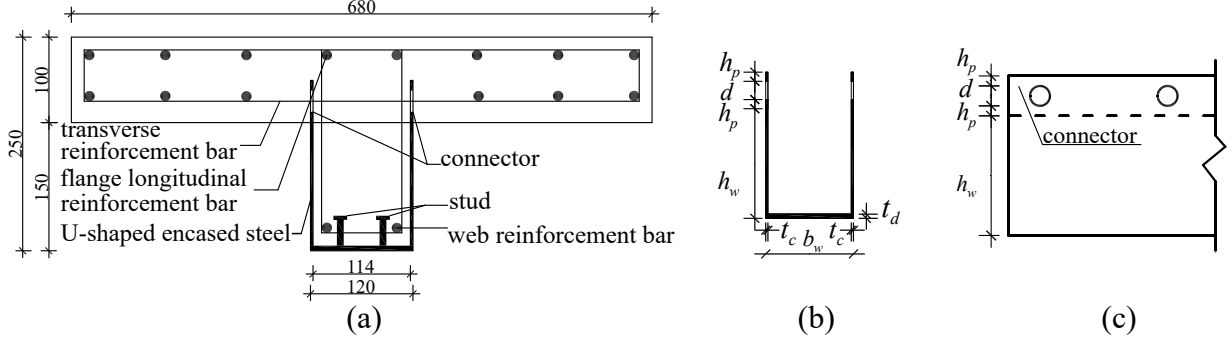


Figure 9: Details of the ZHL1-1 cross-section (dimensions in mm): (a) typical cross-section; (b) U-shaped steel (front view); and (c) U-shaped steel (side view).

As illustrated in Fig. 9(a), the ZHL1-1 section is reinforced using 14 reinforcement bars of 6 mm diameter in the flange, and two reinforcement bars of 6 mm diameter in the web. Figs. 9(b) and (c) show the ZHL1-1 U-shaped steel. The ZHL1-1 U-shaped steel connector section has perforations of 125 mm diameter spaced at 160 mm in the longitudinal direction. When the height of a SUSCCB permits, headed studs may be welded onto the U-shaped steel bottom plate in order to strengthen the connectivity between the U-shaped steel and the concrete web. Here, the bottom headed studs are 50 mm high, and of 16 mm diameter spaced at 160 mm in the longitudinal direction. The concrete compressive strength is 50.8 MPa, as defined for C50 concrete [37].

### 3.1. Load-deflection curves

Load-deflection curves are obtained to investigate the governing parameters and the applicability of simplified plasticity theory discussed in the next section. Table 5 reports the results of the load-deflection curves obtained from the parametric study in terms of yield load  $P_{ny}$ , yield displacement  $\Delta_{ny}$  (data from universal yield moment method [36]), peak load  $P_{nmax}$ , peak displacement  $\Delta_{nx}$ , ultimate load  $P_{nu}$ , and ultimate displacement  $\Delta_{nu}$ . Results are analyzed and discussed in what follows.

#### 3.1.1. U-shaped steel section

The effect of the thicknesses  $t_c$ ,  $t_d$ , and strength  $f_y$  of the U-shaped steel obtained are shown in Figs. 10(a), (b), and (c). The load-deflection curves exhibit a linear ascending behavior, followed by an approximate plateau stage, and terminating by a sudden drop. The ultimate load from these parametric studies has 85% of the peak load, all results exhibit a ductile failure ( $P_{nu} = 0.85P_{nmax}$ ) and the corresponding compressive strains of concrete at both the mid-span and the mid-support are close or larger than the ultimate compressive strain of 0.0033. Fig. 10(a) shows that a SUSCCB with  $t_c = 6$  mm has a 38.8% higher peak load and 10.8% higher initial stiffness than those with  $t_c = 3$  mm. Fig. 10(b) shows that a SUSCCB with  $t_d = 10$  mm has a 25.3% higher peak load and 9.9% higher initial stiffness than that with  $t_d = 6$  mm. Fig. 10(c) shows that the flexural capacity of a SUSCCB with  $f_y = 465$  MPa increases by 55.0% compared with  $f_y = 235$  MPa. This suggests that the thicknesses of U-shaped steel  $t_c$  and  $t_d$  and the strength  $f_y$  are key factors affecting the flexural behavior of a SUSCCB.



Table 4: Varying parameters for the SUSCCB parametric study.

SUSCCB	Parameter		SUSCCB	Parameter	
ZHL1-1		6	ZHL6-A		235
ZHL1-2	$d'_{ys}$ (mm)	10	ZHL6-B	$f'_y = f_y$ (MPa)	345
ZHL1-3		14	ZHL6-C		390
ZHL2-1	$d_{ys}$ (mm)	10	ZHL7-A		40
ZHL2-2		14	ZHL7-B	$f_{cu}$ (MPa)	45
ZHL3-A		235	ZHL7-C		60
ZHL3-B	$f'_{ys} = f_{ys}$ (MPa)	300	ZHL7-D		65
ZHL3-C		335	ZHL8-1	$h_f$ (mm)	80
ZHL4-1		4	ZHL8-2		120
ZHL4-2	$t_c$ (mm)	5	ZHL9-1	$b_f$ (mm)	660
ZHL4-3		6	ZHL9-2		700
ZHL5-1		8	ZHL10-1	$h_w$ (mm)	140
ZHL5-2	$t_d$ (mm)	9	ZHL10-2		160
ZHL5-3		10	ZHL11-1	$b_w$ (mm)	110
			ZHL11-2		130

ZHL1-1 is the SUSCCB number, details of the ZHL1-1 cross-section are shown in Fig. 9, the other cross sections are the same as ZHL1-1 except for the varying parameters indicated;

$d'_{ys}$  and  $d_{ys}$  are the longitudinal reinforcement bar diameters in the flange top and web, respectively;

$f'_{ys}$  and  $f_{ys}$  are the compressed and tensile strengths of longitudinal reinforcement bars, respectively;

$t_c$  and  $t_d$  are the thicknesses of the steel lateral plate and bottom plate, respectively;

$f'_y$  and  $f_y$  are the compressed and tensile strengths of the steel, respectively;

$f_{cu}$  is the standard value of concrete cube compressed strength;

$b_f$  and  $h_f$  are the width and depth of the flange, respectively;

$b_w$  and  $h_w$  are the width and depth of the web, respectively.

Table 5: Results of load-deflection curves from the parametric study.

SUSCCB	$P_{ny}$ (kN)	$\Delta_{ny}$ (mm)	$P_{nmax}$ (mm)	$\Delta_{nx}$ (mm)	$P_{nu}$ (kN)	$\Delta_{nu}$ (kN)
ZHL1-1	110.2	7.8	312.8	50.8	265.9	65.3
ZHL1-2	128.1	8.1	321.6	56.6	273.4	65.4
ZHL1-3	148.4	8.2	329.3	68.9	279.9	77.5
ZHL2-1	115.9	8	322.1	50.4	273.8	66.1
ZHL2-2	119.3	8.2	335.6	48.6	285.2	60.4
ZHL3-A	100.1	7	300.5	49.5	255.4	55.3
ZHL3-B	104.4	7.3	306.6	49	260.6	58.4
ZHL3-C	109.7	7.5	309.2	50.2	262.8	63.1
ZHL4-1	123.1	8.3	354.8	49.3	301.6	68.4
ZHL4-2	128.6	8.5	395.6	52	336.3	66.3
ZHL4-3	134.3	8.7	434.3	59.5	369.2	68.9
ZHL5-1	121.4	8.2	352.6	52.6	299.7	66.4
ZHL5-2	127.5	8.4	372	53.4	316.2	68.5
ZHL5-3	132.2	8.6	391.7	54.6	332.9	70.1
ZHL6-A	107.2	7.7	201.8	17.3	171.5	20.4
ZHL6-B	108.9	7.8	242.7	36.1	206.3	40.5
ZHL6-C	109.3	7.8	275.4	46.2	234.1	49.8
ZHL7-1	110.3	7.9	309.5	53.2	263.1	60.3
ZHL7-2	107.9	7.7	311.6	53.3	264.8	61.4
ZHL7-3	110	7.9	314.7	50.6	267.5	60.9
ZHL7-4	108.9	7.8	316.9	47.6	269.4	59.8
ZHL8-1	117.4	7.6	272.6	58.6	231.7	63.4
ZHL8-2	125.8	8.1	346.4	50.5	294.4	61.5
ZHL9-1	110.5	7.9	311.1	50	264.5	58.5
ZHL9-2	110.3	7.9	314.9	52.9	267.6	59.9
ZHL10-1	118.3	7.9	295.5	52.6	251.1	58.9
ZHL10-2	124.3	8.2	329.3	50.2	279.9	61.3
ZHL11-1	109.4	7.6	302.3	52.4	256.9	61.8
ZHL11-2	121.2	8.1	323.3	49.6	274.8	55.5

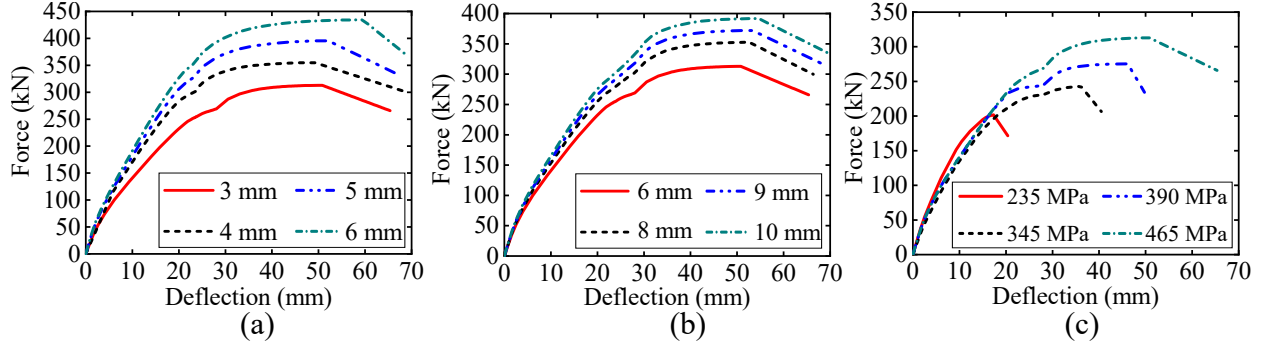


Figure 10: Comparison of load-deflection curves with varying steel section dimensions and its strength: (a) varying lateral thickness,  $t_c$ ; (b) varying bottom thickness,  $t_d$ ; and (c) varying steel strength,  $f_y$ .

### 3.1.2. Longitudinal reinforcement bars

Fig. 11 investigates the effects of varying the longitudinal reinforcement bar sizes in the web and top of the flange, and of varying their strength. The load-deflection curves exhibit a similar behavior to those shown in Fig. 10.

Typically, the cross-section area of U-shaped steel is much larger than that of reinforcement bars in a SUSCCB usually, hence the influence of reinforcement bar diameter may not be significant (Fig. 11(a) and (b)). However, the diameter of the reinforcement bars has a clear effect on the flexural capacity (Fig. 11(a) and (b)). From Fig. 11(c), one can observe that varying the strength of the reinforcement bar yields a similar initial stiffness while the flexural capacity is different. This suggests that the diameter and strength of a reinforcement bar ( $f'_{ys} = f_{ys}$ ) are key factors affecting the flexural behavior of a SUSCCB.

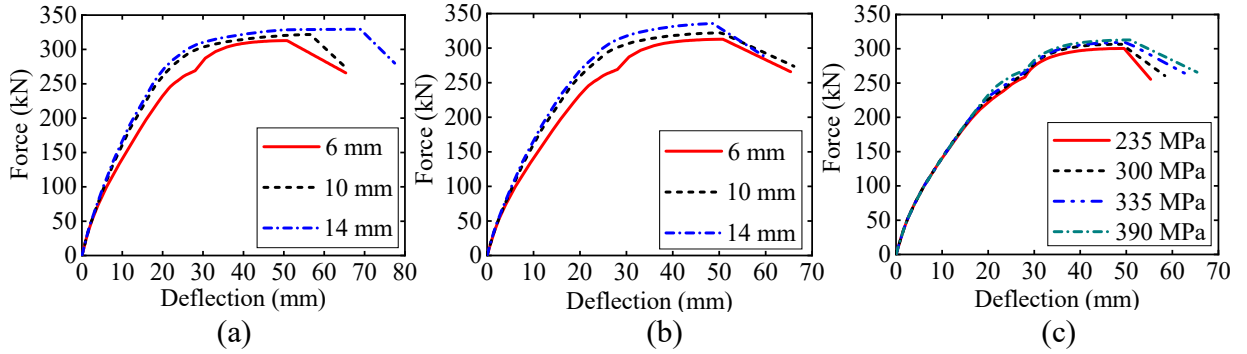


Figure 11: Comparison of load-deflection curves with varying longitudinal rebar sizes in the web and top of the flange, and varying strength: (a) varying the flange top rebar diameters,  $d'_{ys}$ ; (b) varying web rebar diameters,  $d_{ys}$ ; and (c) varying rebar strength,  $f'_{ys} = f_{ys}$ .

### 3.1.3. Concrete strength

The effect of the concrete strength on the SUSCCB is investigated in Fig. 12. The increase of the concrete strength does not have much influence on the load-deflection curves. The ultimate flexural capacity and stiffness increase slightly with the increase of concrete strength. Additionally, the ductility decreases as the concrete strength increases. This shows that increasing the strength of the concrete does not significantly improve the mechanical properties of the SUSCCB.

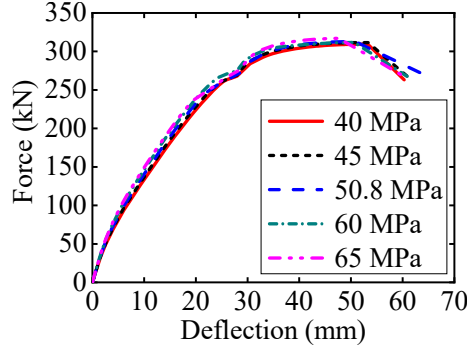


Figure 12: Comparison of load-deflection curves with varying concrete strength.

#### 3.1.4. Flange and web sizes

Figs. 13(a) and (b) show the effect of flange depth and width on the load-deflection curves. Increasing the depth of the flange greatly improves the mechanical performance of the SUSCCB. The flange depth of 100 mm and 120 mm have higher initial stiffnesses of 10.9% and 11.2%, respectively, and higher peak loads of 14.8% and 27.1%, respectively, compared to the 80 mm-deep section. However, changing the width of the flange results in similar stiffness and capacity. Since the flange of the T-section is in the tensile zone, the tensile action of the concrete flange after cracking is almost negligible when the intermediate support T-section fails at the ultimate state of the flexural capacity controlled by the negative bending moment at the intermediate support of the two-span continuous composite beam.

Figs. 13(c) and (d) show the effect of varying web depth and width on the load-deflection curves. Increasing the width and depth of the web greatly improves the mechanical performance of the SUSCCB. The web depths of 150 mm and 160 mm have higher initial stiffnesses of 7.5% and 7.9%, respectively, and higher peak loads of 5.9% and 11.5%, respectively, compared to the 140 mm-deep section. The web widths of 120 mm and 130 mm have higher initial stiffnesses of 4.8% and 5.1%, respectively, and higher peak loads of 3.5% and 7.0%, respectively, compared to the 110 mm-wide section.

Results suggest that flange and web depths ( $h_f$ ,  $h_w$ ), and web width ( $b_w$ ) are key factors affecting the flexural behavior of a T-section SUSCCB controlled by the negative bending moment.

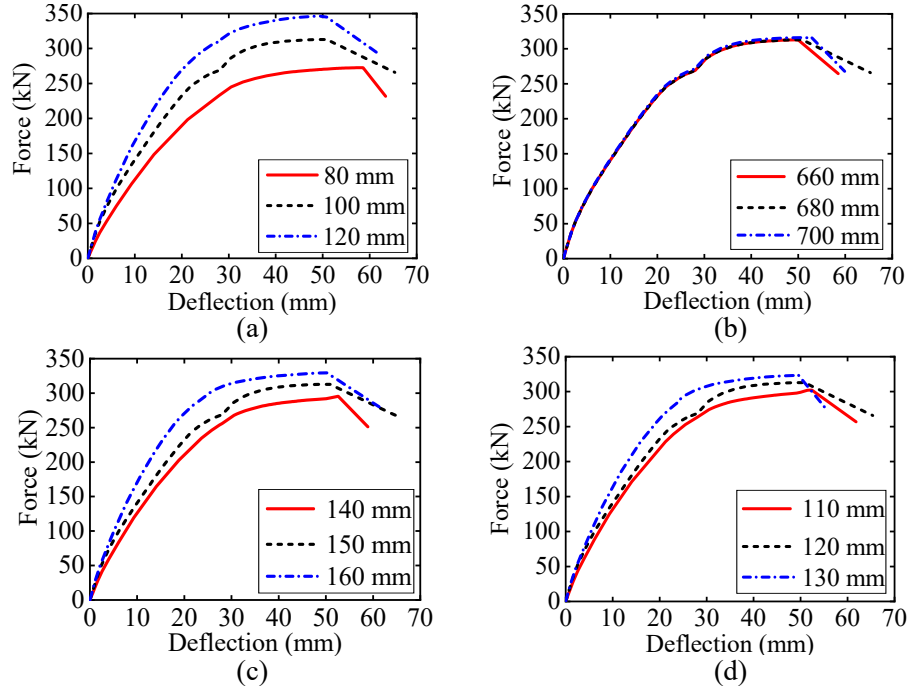


Figure 13: Comparison of load-deflection curves with varying flange and web sizes: (a) varying flange depth,  $h_f$ ; (b) varying flange width,  $b_f$ ; (c) varying web depth,  $h_w$ ; and (d) varying web width,  $b_w$ .

To summarize, the key parameters affecting the flexural behavior of a T-section SUSCCB controlled by the negative bending moment are the reinforcement bar diameters in the top of the flange and web, reinforcement bar strengths, thicknesses of lateral and bottom plates, steel strength, concrete strength, flange and web depths, and web width. Increasing the value of these parameters increases the flexural capacity. The flange width does not have a significant effect on capacity.

### 3.2. Stress and strain analyses

Stress and strain analyses are conducted to investigate the limit state of the flexural capacity. Results are analyzed and discussed in what follows.

#### 3.2.1. Stress analysis

Eight points are selected to assess performance through stress analysis: the intersection, bottom edge, maximum stressed reinforcement bar in tension, and maximum stressed reinforcement bar in compression at the mid-span and the mid-support (Support B). The intersection denotes the intersection point of the U-shaped steel plate and concrete flange, and the bottom edge denotes the bottom edge of the U-shaped steel plate.

Figs. 14(a) and (b) show the stresses from the intersections and bottom edge at the mid-span and mid-support (Support B). The intersections at the mid-support start to yield in tension (465 MPa) when the beam is displaced by 18.6 mm. At mid-span, the steel bottom edge yields in tension at 19.5 mm displacement, and the intersections start to yield in compression at 44.6 mm displacement. When the beam surpasses the peak load of 312.8 kN (at a displacement of 50.8 mm), the stress of the mid-support at the steel bottom edge is 138.7 MPa. Note that the yield stress for U-shaped steel is 465 MPa, indicating that it remains compressive and elastic.

Figs. 14(c) and (d) show the reinforcement bar stresses in compression and tension at the mid-span and mid-support. The reinforcement bars of 6 mm diameter yield at 390 MPa. As observable from the figure, all of these reinforcement bars yield in compression and in tension around a similar point in the early stage

(i.e., the mid-support and mid-span yield in tension at 15.9 mm and 23.1 mm, and yield in compression at 16.1 mm and 18.6 mm, respectively). It follows that the strength of the longitudinal reinforcement bars is fully utilized during the pure bending region.

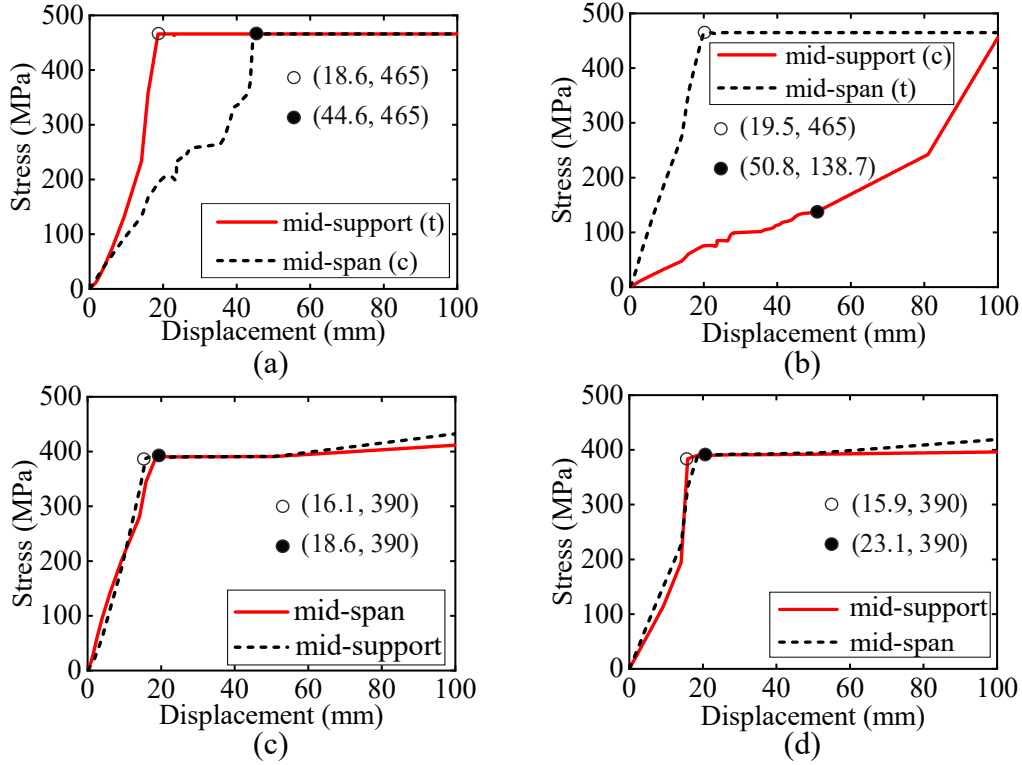


Figure 14: Stress versus loading displacement curves of ZHL 1-1 (compressive, c; tensile, t; stress values are absolute values): (a) the stresses from the intersection at mid-span and mid-support; (b) the stresses from the bottom edge at mid-span and mid-support; (c) the rebar stresses in compression at mid-span (top rebar in flange) and mid-support (rebars in web); and (d) the rebar stresses in tension at mid-span (rebars in web) and mid-support (top rebar in flange).

### 3.2.2. Strain analysis

The compressive strain-loading displacement curves from the edges of the compressive concrete at mid-span and mid-support are plotted in Fig. 15(a). When the loading displacement has reached its peak displacement at 50.8 mm, the edge compressive concrete strains at mid-span and mid-support are 0.0034 and 0.0032, respectively. According to the Code for the design of concrete structures, the peak compressive strain of C50 concrete is 0.002 and the ultimate compressive strain of C50 concrete is 0.0033 [37]. Thus, the compressive strains of concrete at both the mid-span and the mid-support have exceeded the peak compressive strain of 0.002, and are close or larger than the ultimate compressive strain of 0.0033.

The typical longitudinal strain distributions along the section height versus the loading displacement at mid-span and mid-support are shown in Figs. 15(b) and (c). During the initial linear ascending stage, the strains along the section height are linearly distributed, indicating that the Bernoulli-Euler beam theory is satisfied. As the loading displacement continues to increase, the strains along the section height at mid-support are still linearly distributed. However, the strain distribution along the section height at mid-span exhibits a parabolic shape, and the Bernoulli plane assumption is basically satisfied.

In summary, except for the bottom edge of the U-shaped steel plate at mid-support that is compressed and unyielded, all components have reached their yield strength or peak compressive stain at the peak load, indicating that most of the SUSCCB materials have been fully utilized. It can also be stated that SUSCCBs approximately satisfy the Bernoulli plane assumption.

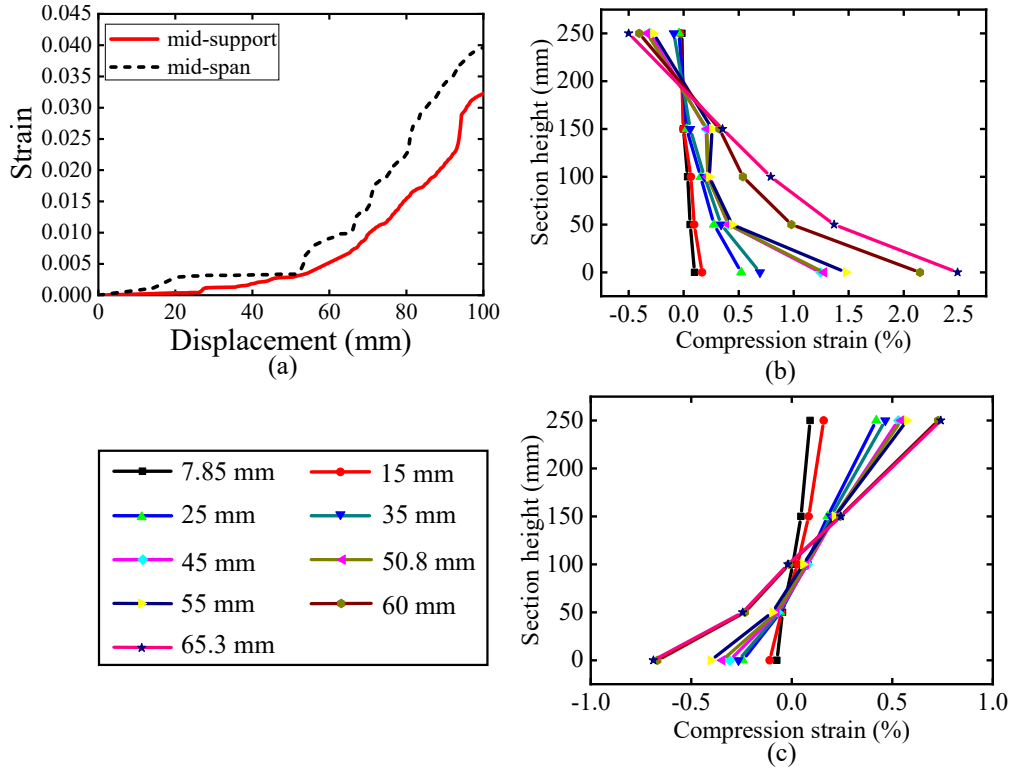


Figure 15: Strain distribution versus loading displacement of ZHL 1-1: (a) strains from the edges of the compressive concrete at mid-span and mid-support; (b) strain distributions along the section height at mid-span; and (c) strain distributions along the section height at mid-support.

### 3.3. Comparison of SUSCCB and VUSCCB

The ZHL 1-1, ZHL 1-2 and ZHL 1-3 specimens are selected to compare the performance of the SUSCCB system against the data simulated on the VUSCCB B1, B2 and B3. From the load-deflection curve results listed in Table 6 and plotted Fig. 16, the initial stiffnesses, bearing capacities and peak displacements of the ZHL 1-1, ZHL 1-2, and ZHL 1-3 specimens are higher than those of the B1, B2 and B3 specimens except at the peak displacement for the ZHL 1-1. The ZHL 1-1 bearing capacity is 4.9% larger than that of the B1 specimen, with the maximum bearing capacity difference between the ZHL 1-1 and the B1 specimens. The ZHL 1-3 peak displacement is 37.3% larger than that of the B3 specimen, with the maximum peak displacement difference between the ZHL 1-3 and the B3 specimens. However, the ZHL 1-1 and ZHL 1-3 specimens utilize 0.2% less steel than the B1 and B3 specimens, and are built with a simpler configuration, which effectively eliminates the stress concentration experienced by the varus steel plate flanges in the VUSCCB.

## 4. Theoretical calculations

This section presents the theoretical calculation of the flexural capacity of the new SUSCCB. First, the assumptions are presented. Second, the theoretical flexural capacity is calculated based on the simplified plastic theory considering two conditions in the positive or negative moment sections: when the neutral axis is located in the flange, and when the neutral axis is located in the U-section. Lastly, the theoretical values are compared with the simulation results.

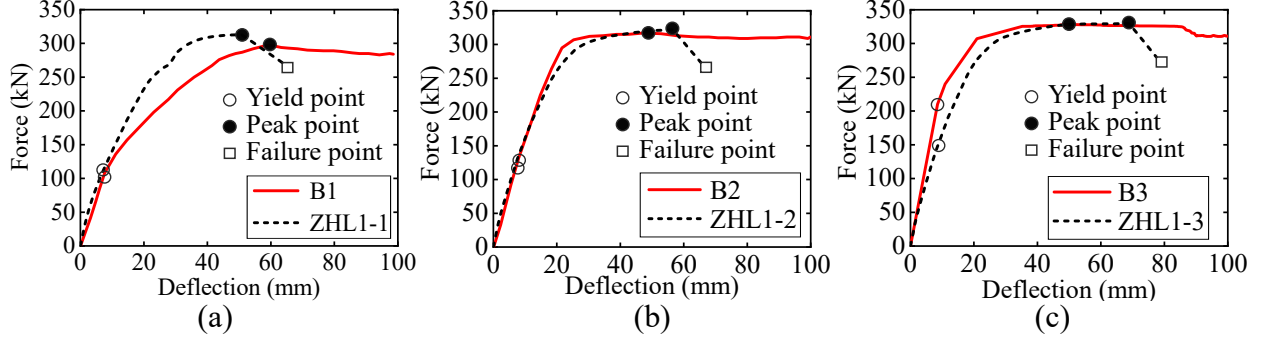


Figure 16: Comparisons of load-deflection curves between: (a) B1 and ZHL1-1; (b) B2 and ZHL1-2; and (c) B3 and ZHL1-3.

Table 6: Comparison of ZHL1-1 and B1.

USCCB NO.	Steel ratio (%)	Yield load (kN)	Yield displacement (mm)	Peak load (kN)	Peak displacement (mm)	Failure load (kN)	Failure displacement (mm)
B1	2.3	100.7	8.3	298.2	59	-	-
ZHL1-1	2.1	110.2	7.9	312.8	50.8	265.9	65.3
B2	2.3	130.2	8.3	315.1	52.9	-	-
ZHL1-2	2.1	128.1	8.1	321.6	56.6	273.4	65.4
B3	2.3	215.9	9.4	328	50.2	-	-
ZHL1-3	2.1	148.4	8.2	329.3	68.9	279.9	77.5

#### 4.1. Assumptions

Based on the load-deflection results of the SUSCCB simulations, the flexural capacity of a SUSCCB can be calculated based on the simplified plastic theory with the following assumptions:

1. The shear connection between the flange and the web can fully carry the flexural capacity of a SUSCCB section.
2. The strain plane cross-section is satisfied during the entire bending process (see Section 3.2.2).
3. Without considering the tensile action of concrete after cracking, the concrete compressive stress can be simplified into a rectangular stress distribution that has reached the design value of the axial compressive strength (see Section 3.2.2).
4. According to the position of the plastic neutral axis, the U-shaped steel and reinforcement bars of a SUSCCB section may be partially pulled and partially compressed, but all of them are assumed to carry a uniform stress and reach the design values of tensile or compressive strengths of steel and reinforcement bars (see Section 3.2.1).

#### 4.2. Theoretical analysis of the flexural capacity

##### 4.2.1. Positive moment $M_u$

Different plastic theoretical formulas for calculating the flexural capacity of a new SUSCCB can be derived as a function of the position of the stress neutral axis in positive moment section. When the plastic neutral axis is in the flange and between the connector section and the concrete edge in positive moment section, as shown in Fig. 17:

$$f_c b_f (h_f - h_{pbl}) + f'_{ys} A'_{ys} > f_y A_p + f_y A_s + f_{ys} A_{ys} \quad (1)$$



where  $f_c$  is the concrete compressive strength;  $b_f$  and  $h_f$  are the width and depth of the flange, respectively;  $h_{pbl}$  is the connector batten height,  $h_{pbl} = 2h_p + d$ ;  $h_p$  is the height of the top or lower batten of the connector,  $d$  is the opening diameter of connector batten;  $A_{ys}$  and  $A'_{ys}$  are the reinforcement bars' area in the web and the top reinforcement bars' area in the flange, respectively;  $f_{ys}$ ,  $f'_{ys}$  are the tensile and compressed yield strengths of the reinforcement bars, respectively;  $f_y$  is the tensile yield strength of the U-shaped steel;  $A_p$  is the total area of upper battens of connector ( $A_p = 2t_c h_p$ );  $A_s$  is the additive area of the U-shaped steel plate and the lower battens of connector ( $A_s = 2t_c(h_w + h_p - t_d) + t_d b_w$ );  $b_w$  and  $h_w$  are the width and depth of the web, respectively;  $t_c$  and  $t_d$  are the thicknesses of side and bottom panels of the U-shaped steel.

Define the height and area of the compressive concrete  $x$  and  $A_c = b_f x$ . The compressive resistance of the compressed concrete becomes  $f_c b_f x = f_c A_c$ , the compressive resistance of the compressed top reinforcement bars in the flange becomes  $A'_{ys} f'_{ys}$ , the tensile resistance of the longitudinal reinforcement bars in the web becomes  $f_{ys} A_{ys}$ , the tensile capacity of the U-shaped steel in the web and the lower battens of connector becomes  $f_y A_s$ , and the resultant force of the total area of the upper battens of connector becomes  $f_y A_p$ . It follows that the total resultant force in the beam section is:

$$f_c A_c = f_y A_p + f_y A_s + f_{ys} A_{ys} - f'_{ys} A'_{ys} \quad (2)$$

Take  $y_1$  being the distance from the resultant force  $f_c A_c$  to the resultant force  $f_{ys} A_{ys}$ ,  $y_2$  being the distance from the resultant force  $f'_{ys} A'_{ys}$  to the resultant force  $f_{ys} A_{ys}$ ,  $y_3$  being the distance from the resultant force  $f_y A_p$  to the resultant force  $f_{ys} A_{ys}$ , and  $y_4$  being the distance from the resultant force  $f_y A_s$  to the resultant force  $f_{ys} A_{ys}$ , the flexural capacity  $M_u$  in the positive moment section becomes:

$$M \leq M_u = f_c A_c y_1 + f'_{ys} A'_{ys} y_2 - f_y A_p y_3 - f_y A_s y_4 \quad (3)$$

where  $M$  is the normal section bearing positive bending moment.

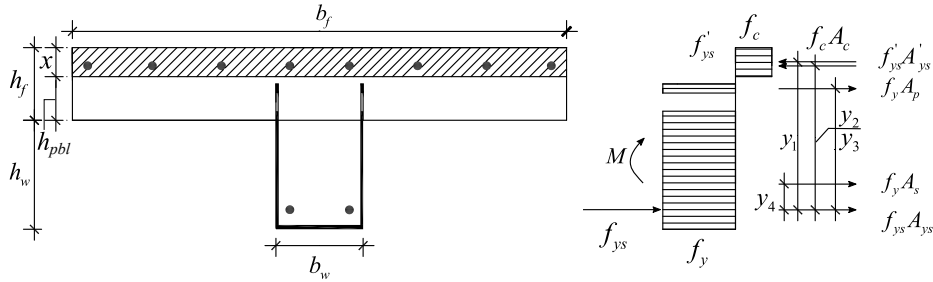


Figure 17: Model for calculating the flexural capacity with the plastic neutral axis in the flange in positive moment section.

When the plastic neutral axis is located in the web in positive moment section, as shown in Fig. 18

$$f_y A_s + f_{ys} A_{ys} > f_c b_f h_f + f'_y A_p + f'_{ys} A'_{ys} \quad (4)$$

where  $f'_y$  is the compressive yield strength of the U-shaped steel.

Define the compressive concrete area  $A_c = b_f h_f + (x - h_f) b_w$ , with  $A'_s$  being the additive compressive area of the U-shaped steel and the lower battens of the connector. The compressive resistance of the compressed concrete becomes  $f_c A_c$ , the compressive resultant force of the total area of the upper battens of connector becomes  $f'_y A_p$ , the compressive resistance of the compressed top reinforcement bars of the flange becomes  $f'_{ys} A'_{ys}$ , the compressive resistance of the total compressive area of the U-shaped steel and the lower battens of the connector becomes  $f'_y A'_s$ , the tensile resistance of the longitudinal reinforcement bars of the web becomes  $f_{ys} A_{ys}$ , and the tensile capacity of the U-shaped steel in the web becomes  $f_y (A_s - A'_s)$ . It follows that the resultant force in the beam section is:

$$f_c A_c + f'_y A_p + f'_y A'_s + f'_{ys} A'_{ys} = f_y (A_s - A'_s) + f_{ys} A_{ys} \quad (5)$$

Take  $y_a$  being the distance from the resultant force  $f'_{ys}A'_{ys}$  to the resultant force  $f_{ys}A_{ys}$ ,  $y_b$  is the distance from the resultant force  $f'_yA'_p$  to the resultant force  $f_{ys}A_{ys}$ ,  $y_c$  is the distance from the resultant force  $f_cA_c$  to the resultant force  $f_yA_s$ ,  $y_d$  is the distance from the resultant force  $f'_{ys}A'_{ys}$  to the resultant force  $f_{ys}A_{ys}$ , and  $y_e$  is the distance from the resultant force  $f_y(A_s - A'_s)$  to the resultant force  $f_yA_s$ . The flexural capacity  $M_u$  in the positive moment section becomes:

$$M \leq M_u = f'_{ys}A'_{ys}y_a + f'_yA'_py_b + f_cA_cy_c + f'_yA'_sy_d - f_y(A_s - A'_s)y_e \quad (6)$$

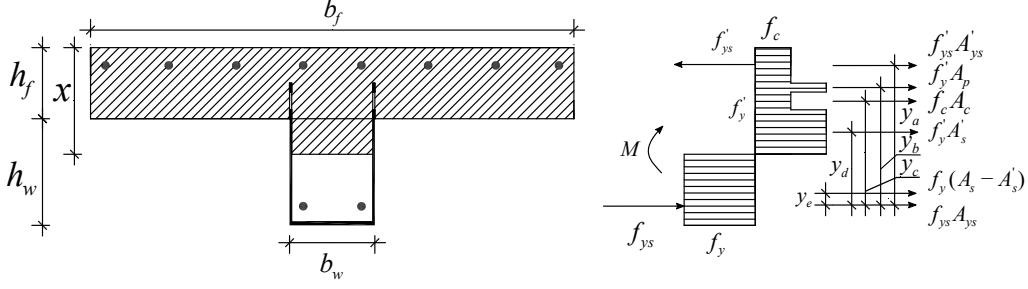


Figure 18: Model for calculating the flexural capacity with the plastic neutral axis in the web in positive moment section.

The calculated theoretical flexural capacities ( $M_{uIDA}$ ) in the positive moment section are compared with the simulation results ( $M_{uFEA}$ ) listed in Table 7. It can be observed that analytical values have a good agreement with the simulation results with relative errors of less than 5%. It follows that the simplified plastic theory can be used to calculate the flexural capacity of a SUSCCB. Additionally, one can observe that only four of the  $M_{uIDA}/M_{uFEA}$  ratios are above 1, with the remaining 25 (86.2% of the number of ratios) being less than 1. The theoretically calculated value is slightly overestimated when using the simplified complete plastic theory. When a SUSCCB reaches the limit state of the flexural capacity, the monolithic steel U-section and concrete are not completely plastic near the neutral axis.

Table 7: Comparison values between design calculation value and related simulation value in the positive moment section.

SUSCCB	$M_{u,FEA}$ (kN·m)	$M_{u,IDA}$ (kN·m)	$\delta$
ZHL1-1	147.2	149.5	0.02
ZHL1-2	153.6	157.1	0.02
ZHL1-3	163.6	167.6	0.02
ZHL2-1	154	156.9	0.02
ZHL2-2	163.3	167.1	0.02
ZHL3-A	143.6	147.6	0.03
ZHL3-B	143	148.4	0.04
ZHL3-C	144.2	148.8	0.03
ZHL4-1	169.3	169.4	0
ZHL4-2	189.7	188.4	-0.01
ZHL4-3	210.3	206.5	-0.02
ZHL5-1	171.1	173.7	0.02
ZHL5-2	182.5	185.6	0.02
ZHL5-3	193.9	197.5	0.02
ZHL6-A	89.8	91.9	0.02
ZHL6-B	111.9	114.3	0.02
ZHL6-C	121.1	127.5	0.05
ZHL7-1	147.2	146.2	-0.01
ZHL7-2	147.8	147.9	0
ZHL7-3	148	151.3	0.02
ZHL7-4	148.7	152.1	0.02
ZHL8-1	129.7	132.9	0.02
ZHL8-2	167.6	166.1	-0.01
ZHL9-1	146.7	149.2	0.02
ZHL9-2	147.8	149.8	0.01
ZHL10-1	138	140	0.01
ZHL10-2	156.3	159.3	0.02
ZHL11-1	141.6	143.4	0.01
ZHL11-2	152.8	155.6	0.02

#### 4.2.2. Negative moment $M_{nu}$

When the plastic neutral axis is located in the web in the negative moment section, as shown in Fig. 19:

$$f_c b_w h_w + f'_y (A_s - A_p) + f'_{ys} A_{ys} > 2f_y A_p + f_{ys} A'_{ys} \quad (7)$$

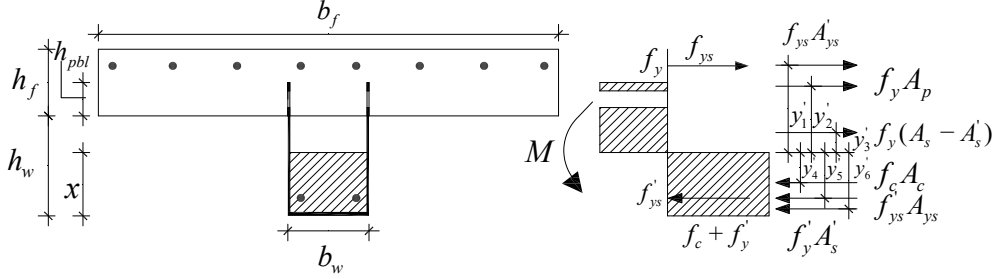


Figure 19: Model for calculating the flexural capacity with the plastic neutral axis in the web in the negative moment section.

Define the height and area of the compressive concrete  $x$  and  $A_c = x b_w$ ,  $A'_s = b_w t_d + 2x t_c$  is the compressive area of the U-shaped steel plate. It follows that the total resultant force in the beam section is:

$$f_c A_c + f'_y A'_s + f'_{ys} A_{ys} = f_y A_p + f_y (A_s - A'_s) + f_{ys} A'_{ys} \quad (8)$$

The flexural capacity  $M_{nu}$  in negative moment section becomes:

$$M \leq M_{nu} = f_{ys} A'_{ys} y'_1 + f_y A_p y'_2 + f_y (A_s - A'_s) y'_3 + f_c A_c y'_4 + f'_{ys} A_{ys} y'_5 - f'_y A'_s y'_6 \quad (9)$$

where  $y'_1$  is the distance from the resultant force  $f_{ys} A'_{ys}$  to the plastic neutral axis,  $y'_2$  is the distance from the resultant force  $f_y A_p$  to the plastic neutral axis,  $y'_3$  is the distance from the resultant force  $f_y (A_s - A'_s)$  to the plastic neutral axis,  $y'_4$  is the distance from the resultant force  $f_c A_c$  to the plastic neutral axis,  $y'_5$  is the distance from the resultant force  $f'_{ys} A_{ys}$  to the plastic neutral axis, and  $y'_6$  is the distance from the resultant force  $f'_y A'_s$  to the plastic neutral axis.

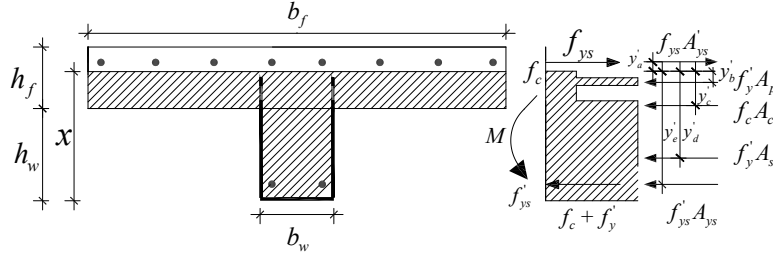


Figure 20: Model for calculating the flexural capacity with the plastic neutral axis in the flange in the negative moment section.

When the plastic neutral axis is in the flange and between the connector section and the concrete edge in the negative moment section, as shown in Fig. 20:

$$f_c b_w h_w + f'_y (A_s - A_p) + f'_{ys} A_{ys} < 2f_y A_p + f_{ys} A'_{ys} \quad (10)$$

Define the height and area of the compressive concrete  $x$  and  $A_c = b_w h_w + (x - h_w) b_f$ . It follows that the total resultant force in the beam section is:

$$f_c A_c + f'_{ys} A_{ys} + f'_y A_p + f'_y A_s = f_{ys} A'_{ys} \quad (11)$$

Table 8: Comparison values between design calculation value and related simulation value in the negative moment section.

SUSCCB	$M_{nu,FEA}$ (kN·m)	$M_{nu,IDA}$ (kN·m)	$\delta$
ZHL1-1	67.3	72.4	0.07
ZHL1-2	115.4	120.5	0.04
ZHL1-3	172.5	176.5	0.02
ZHL2-1	68.5	72.5	0.06
ZHL2-2	69.3	72.4	0.04
ZHL3-A	58.4	60.3	0.03
ZHL3-B	66.6	65.4	-0.02
ZHL3-C	67.2	68.2	0.01
ZHL4-1	78.5	82.2	0.05
ZHL4-2	85.5	91.3	0.06
ZHL4-3	95.4	99.9	0.05
ZHL5-1	68.5	74.9	0.09
ZHL5-2	72.8	76.1	0.04
ZHL5-3	72.7	77.4	0.06
ZHL6-A	52.5	52.6	0.00
ZHL6-B	58.4	62.1	0.06
ZHL6-C	64.5	66.0	0.02
ZHL7-1	69.8	71.8	0.03
ZHL7-2	65.9	72.1	0.09
ZHL7-3	70.2	72.8	0.04
ZHL7-4	67.0	72.9	0.08
ZHL8-1	64.1	69.3	0.07
ZHL8-2	73.2	75.4	0.03
ZHL9-1	69.9	72.4	0.03
ZHL9-2	66.5	72.4	0.08
ZHL10-1	63.8	66.9	0.05
ZHL10-2	76.1	78.1	0.03
ZHL11-1	64.4	71.4	0.10
ZHL11-2	66.2	73.2	0.10

where  $y'_a$  is the distance from the resultant force  $f_{ys}A'_{ys}$  to the plastic neutral axis,  $y'_b$  is the distance from the resultant force  $f'_yA_p$  to the plastic neutral axis,  $y'_c$  is the distance from the resultant force  $f_cA_c$  to the plastic neutral axis,  $y'_d$  is the distance from the resultant force  $f'_yA_s$  to the plastic neutral axis, and  $y'_e$  is the distance from the resultant force  $f'_{ys}A_{ys}$  to the plastic neutral axis. The flexural capacity  $M_{nu}$  in the negative moment section becomes:

$$M \leq M_{nu} = f_{ys}A'_{ys}y'_a + f'_yA_py'_b + f_cA_cy'_c + f'_yA_sy'_d + f'_{ys}A_{ys}y'_e \quad (12)$$

The calculated theoretical flexural capacities ( $M_{nu,IDA}$ ) in negative moment section are compared with the simulation results ( $M_{nu,FEA}$ ) listed in Table 8. It can be observed that analytical values have a good agreement with simulation results, with relative errors less than 5%. It follows that the simplified plastic theory can be used to calculate the flexural capacity of a SUSCCB.

## 5. Conclusion

This paper proposed a novel SUSCCB, engineered to overcome challenges with the existing varus-type or valgus-type USCCB. The SUSCCB is constituted by encasing the top sections of the U-shaped steel plates directly into the concrete flange, with the composite action generated through perfobond connections

consisting of reinforcement bars transversely passing through perforations in the encased top sections of the steel plates. A FEM was developed to conduct a performance analysis of the SUSCCB, first validated against experimental results obtained on three VUSCCB experimental specimens. The validated FEM was applied to the study of the proposed SUSCCB to conduct a parametric study. A comparison between the SUSCCB and VUSCCB systems was performed and numerical results on the SUSCCB normal section's stresses and strains were analyzed. It was found that based on the load-deflection results, the flexural capacity of a SUSCCB can be calculated by the simplified plastic theory. The primary findings of the study can be summarized as follows:

1. Compared against VUSCCBs, the proposed SUSCCB has many advantages: for similar section area of reinforcement bars and U-shaped steel, the capacity and initial stiffness are higher, and the SUSCCB requires fewer welds and it is therefore simpler, faster, and thus less expensive to fabricate.
2. Key parameters affecting the flexural behavior of a SUSCCB controlled by the negative bending moment are longitudinal reinforcement bars, thicknesses of steel, strength of steel, strength of concrete, depths of flange and web, and width of web. Of all the influencing factors, the lateral thickness of steel is the most important, the influence of longitudinal reinforcement bar diameter on section area is not significant, and the concrete strength does not have a substantial effect. The flange width does not have a significant effect on capacity for a T-section undergoing negative bending moment.
3. Euler beam assumption is satisfied when the SUSCCB is subjected to bending. When a SUSCCB reaches the limit state of the flexural capacity, most of the SUSCCB materials are yielded, and the plasticity of the compressed concrete is very obvious, with the edge strain of the compressed concrete being close to or exceeding the ultimate compressive concrete strain. It follows that the flexural capacity of a SUSCCB can be calculated according to the simplified plastic theory.

## Acknowledgments

The authors are grateful to the support provided by the National Natural Science Foundation of China (grant numbers 51878663).

## References

- [1] B. Hu, Study on mechanical properties of the u-steel encased concrete composite beams, Master's thesis, The University of Guangzhou, China (2016).
- [2] H. Han, J. Huang, P. Li, G. Zhao, Z. Lv, Y. Lou, Design of gigantic transition beams for r.c.tower building of beijing yintai center, *Journal of Building Structure* (2007).
- [3] Z. Zhang, C. Huang, H. Xu, Force transfer mechanism for steel-concrete composite structures of hybrid cable-stayed bridges, *Journal of Huazhong University of Science and Technology(Natural Science Edition)* (2010).
- [4] K. M. A. Hossain, Experimental & theoretical behavior of thin walled composite filled beams (2003).
- [5] K. M. A. Hossain, Designing thin-walled composite-filled beams, *Proceedings of the Institution of Civil Engineers - Structures and Buildings* 158 (4) (2005) 267–278. doi:10.1680/stbu.2005.158.4.267.
- [6] S. ichi Nakamura, New structural forms for steel/concrete composite bridges, *Structural Engineering International* 10 (1) (2000) 45–50. doi:10.2749/101686600780620955.
- [7] S. ichi Nakamura, Bending behavior of composite girders with cold formed steel u section, *Journal of Structural Engineering* 128 (9) (2002) 1169–1176. doi:10.1061/(asce)0733-9445(2002)128:9(1169).
- [8] L. Lee, S. Quek, K. Ang, Negative moment behaviour of cold-formed steel deck and concrete composite slabs, *Journal of Constructional Steel Research* 57 (4) (2001) 401–415. doi:10.1016/s0143-974x(00)00023-7.
- [9] B. Uy, M. Bradford, Local buckling of cold formed steel in composite structural elements at elevated temperatures, *Journal of Constructional Steel Research* 34 (1) (1995) 53–73. doi:10.1016/0143-974x(94)00021-9.
- [10] B. Uy, M. Bradford, Elastic local buckling of steel plates in composite steel-concrete members, *Engineering Structures* 18 (3) (1996) 193–200. doi:10.1016/0141-0296(95)00143-3.
- [11] T. T. Lie, Fire resistance of circular steel columns filled with bar-reinforced concrete, *Journal of Structural Engineering* 120 (5) (1994) 1489–1509. doi:10.1061/(asce)0733-9445(1994)120:5(1489).
- [12] J. Nie, Y. Xiao, L. Chen, Experimental studies on shear strength of steel-concrete composite beams, *Journal of Structural Engineering* 130 (8) (2004) 1206–1213. doi:10.1061/(asce)0733-9445(2004)130:8(1206).
- [13] A. Boushelham, O. Chaallal, Experimental investigations on the influence of size on the performance of RC t-beams retrofitted in shear with CFRP fabrics, *Engineering Structures* 56 (2013) 1070–1079. doi:10.1016/j.engstruct.2013.06.028.

- [14] G. M. Kotsovou, D. M. Cotsovos, Shear failure criterion for RC t-beams, *Engineering Structures* 160 (2018) 44–55. doi:10.1016/j.engstruct.2017.12.044.
- [15] L.-Z. Chen, G. Ranzi, S.-C. Jiang, F. Tahmasebinia, G.-Q. Li, Behaviour and design of shear connectors in composite slabs at elevated temperatures, *Journal of Constructional Steel Research* 115 (2015) 387–397. doi:10.1016/j.jcsr.2015.08.025.
- 425 [16] S. Al-deen, G. Ranzi, Z. Vrcelj, Shrinkage effects on the flexural stiffness of composite beams with solid concrete slabs: An experimental study, *Engineering Structures* 33 (4) (2011) 1302–1315. doi:10.1016/j.engstruct.2011.01.007.
- [17] J. Qureshi, D. Lam, J. Ye, The influence of profiled sheeting thickness and shear connector's position on strength and ductility of headed shear connector, *Engineering Structures* 33 (5) (2011) 1643–1656. doi:10.1016/j.engstruct.2011.01.035.
- 430 [18] E. Baran, C. Topkaya, Behavior of steel–concrete partially composite beams with channel type shear connectors, *Journal of Constructional Steel Research* 97 (2014) 69–78. doi:10.1016/j.jcsr.2014.01.017.
- [19] Y. Liu, L. Guo, B. Qu, S. Zhang, Experimental investigation on the flexural behavior of steel-concrete composite beams with u-shaped steel girders and angle connectors, *Engineering Structures* 131 (2017) 492–502. doi:10.1016/j.engstruct.2016.10.037.
- 435 [20] P. Keo, C. Lepourry, H. Somja, F. Palas, Behavior of a new shear connector for u-shaped steel-concrete hybrid beams, *Journal of Constructional Steel Research* 145 (2018) 153–166. doi:10.1016/j.jcsr.2018.01.028.
- [21] J. Liu, Y. Zhao, Y. F. Chen, S. Xu, Y. Yang, Flexural behavior of rebar truss stiffened cold-formed u-shaped steel-concrete composite beams, *Journal of Constructional Steel Research* 150 (2018) 175–185. doi:10.1016/j.jcsr.2018.08.011.
- [22] X. Zhou, Y. Zhao, J. Liu, Y. F. Chen, Y. Yang, Bending experiment on a novel configuration of cold-formed u-shaped steel-concrete composite beams, *Engineering Structures* 180 (2019) 124–133. doi:10.1016/j.engstruct.2018.11.001.
- 440 [23] Y. Zhao, X. Zhou, Y. Yang, J. Liu, Y. F. Chen, Shear behavior of a novel cold-formed u-shaped steel and concrete composite beam, *Engineering Structures* 200 (2019) 109745. doi:10.1016/j.engstruct.2019.109745.
- [24] Y. Zhao, X. Zhou, Y. Yang, J. Liu, Y. F. Chen, Torsional effects of a novel rebar stiffened cold-formed u-shaped steel-concrete composite beam system, *Engineering Structures* (2019) 109920doi:10.1016/j.engstruct.2019.109920.
- 445 [25] Y. Liu, S. Wang, H. Xin, Y. Liu, Evaluation on out-of-plane shear stiffness and ultimate capacity of perfobond connector, *Journal of Constructional Steel Research* (2019) 105850doi:10.1016/j.jcsr.2019.105850.
- [26] Y. Liu, H. Xin, Y. Liu, Experimental and analytical study on shear mechanism of rubber-ring perfobond connector, *Engineering Structures* 197 (2019) 109382. doi:10.1016/j.engstruct.2019.109382.
- [27] J. Di, Y. Zou, X. Zhou, F. Qin, X. Peng, Push-out test of large perfobond connectors in steel–concrete joints of hybrid bridges, *Journal of Constructional Steel Research* 150 (2018) 415–429. doi:10.1016/j.jcsr.2018.09.002.
- 450 [28] Z. Zhang, X. Fan, F. Yang, Q. Meng, Experimental research on section design and internal force redistribution of inverted u-shaped high-strength encased steel and high-strength concrete continuous composite beam, *Journal of Building Structure* (2019). doi:10.19701/j.jzjg.2019.06.010.
- [29] Standard for design of steel structures, Beijing, China Architecture & Building Press, 2017.
- 455 [30] Hibbit, Karlsson, Sorensen, ABAQUS/Standard Analysis User's Manual, Hibbit, Karlsson, Sorensen Inc., USA, 2007.
- [31] Specification for seismic test of buildings, Beijing, China Architecture & Building Press, 2015.
- [32] B. Alfarah, F. López-Almansa, S. Oller, New methodology for calculating damage variables evolution in plastic damage model for RC structures, *Engineering Structures* 132 (2017) 70–86. doi:10.1016/j.engstruct.2016.11.022.
- [33] F. Ding, X. Ying, L. Zhou, Z. Yu, Unified calculation method and its application in determining the uniaxial mechanical properties of concrete, *Frontiers of Architecture and Civil Engineering in China* 5 (3) (2011) 381–393. doi:10.1007/s11709-011-0118-6.
- 460 [34] A. S. Genikomsou, M. A. Polak, Finite element analysis of a reinforced concrete slab-column connection using ABAQUS, in: Structures Congress 2014, American Society of Civil Engineers, 2014. doi:10.1061/9780784413357.072.
- [35] A. Wosatko, J. Pamin, M. A. Polak, Application of damage–plasticity models in finite element analysis of punching shear, *Computers & Structures* 151 (2015) 73–85. doi:10.1016/j.compstruc.2015.01.008.
- 465 [36] R. Park, Ductility evaluation from laboratory and analytical testing, in: Proceedings of the 9th world conference on earthquake engineering, Tokyo-Kyoto, Japan, Vol. 8, 1988, pp. 605–616.
- [37] Code for design of concrete structures, Beijing, China Architecture & Building Press, 2010.